How Much of Monthly Mean Precipitation Variability over Global Land is Associated with SST Anomalies?

Zeng-Zhen Hu[1,*], Arun Kumar[1], Bhaskar Jha[1,2], and Boyin Huang[3]

1. Climate Prediction Center, NCEP/NWS/NOAA, College Park, MD 20740, USA
2. Innovim, Greenbelt, Maryland, USA
3. National Centers for Environmental Information (NCEI), NOAA, Asheville, North Carolina, USA.

*Corresponding author address:
Zeng-Zhen Hu
Climate Prediction Center
NCEP/NWS/NOAA
5830 University Research Court
College Park, Maryland 20740, USA
Zeng-Zhen.Hu@NOAA.GOV

Abstract

The role of sea surface temperature (SST) in determining the predictability of monthly mean precipitation over the global land is assessed by analyzing the Atmospheric Model Intercomparison Project (AMIP)-like simulations forced by observed SST, which provides a benchmark for the impact of SST on the precipitation. The correlations of monthly mean precipitation anomalies between the ensemble mean of the AMIP simulations and observations are dominated by positive values with maxima around 0.3~0.4 in the tropical North Africa along 15°N and northeastern Brazil. The SST forcing for the precipitation variability is mainly associated with the El Niño-Southern Oscillation (ENSO) and in the tropical Indian Ocean. Statistically, positive and negative SST anomalies associated with an ENSO cycle have a comparable influence on precipitation variability over the land.

In addition to the spatial variations, the precipitation responses to SST also vary with season and decade. Pattern correlations are larger in boreal winter than in boreal summer in the Northern Hemisphere, and relatively larger in April-June and September-November in the Southern Hemisphere. The global average of correlation is lower during 1957-1980 and 2000-2018, and higher in between. The interdecadal fluctuation of the pattern correlations is coherent with the interdecadal variation of the amplitude of ENSO.

Keywords: Predictability; Global Land Precipitation; Temporal and Spatial Variations of the SST Influence; ENSO

I. Introduction

Sea surface temperatures (SSTs) in the global oceans, particularly in the tropical Pacific Ocean associated with the El Niño-Southern Oscillation (ENSO), are a major source of global climate variability and predictability on seasonal and interannual time scales (Sarachik and Cane 2010; National Research Council 2010). For example, Ropelewski and Halpert (1987) identified the regions with spatially coherent ENSO-related precipitation variability. They noted that in addition to the local influence of ENSO on the tropical Pacific Ocean basin, some remote regions also had ENSO-related precipitation response. These regions are over Australia, North America, South America, the Indian subcontinent, Africa and Central America. They further indicated that ENSO-related precipitation anomalies occur as early as April through May of the following year.

Such impacts of SST on climate variability are largely the basis for short-term climate prediction. For instance, at the Climate Prediction Center (CPC) of the National Centers for Environmental Prediction (NCEP), ENSO is the key predictor for operational seasonal precipitation prediction over U. S. (O'Lenic et al. 2008; Peng et al. 2012; 2013). On average, seasonal precipitation forecasts over the global land are more accurate during El Niño and La Niña events than during neutral years; and stronger ENSO events lead to higher skill of seasonal climate (Goddard and Dilley, 2005).

In addition to the regional dependence of the impacts of ENSO SST (e.g., Davey et al. 2014), the SST influence varies with season and can be easily overshadowed by other processes, such as internal variability (Deser et al. 2018), and low-frequency variation and global warming trend (Yeh et al. 2018). As a result, the uncertainty of the impact of SST anomaly on climate variability on seasonal and interannual time scales is evident (Deser et al. 2018). Given that precipitation is one of the most important variables of societal relevance, such as droughts and floods, it is necessary to further assess the impact of SST on the variability and predictability of precipitation on seasonal and interannual time scales, as well as examine the seasonal and interdecadal variations of the impact. Further, it is important to identify the regions where precipitation is affected by SST and key/sensitive ocean regions that influence the precipitation variation. Such assessments provide a benchmark for the impact of SST on predictability and variability of precipitation.

In this work, Atmospheric Model Intercomparison Project (AMIP)-like experiments, which are forced by observed SST, are analyzed to quantify the SST influence on variability and predictability of precipitation over the land. In addition to observational analysis and model prediction, the analysis of AMIP experiments complements estimate of the impact of SST on climate variability and predictability (Peng et al. 2000; National Research Council 2010). In this analysis, sources of the predictability of precipitation are attributed, and the most effective ocean regions in influencing the precipitation are identified. Also, the seasonal cycle and interdecadal variations of the SST influence, and the possible connection with ENSO are discussed. The interdecadal variations of the SST influence may provide some clues for the interdecadal variations in the skill of precipitation predictability. The rest of the paper is organized as follows: The data used in this work are introduced in section 2; the spatial variations and temporal fluctuations are shown in sections 3 and 4, respectively. Summary and discussion are given in section 5.

2. Data

To examine the influence of global SST on the predictability and variability of precipitation over the land, AMIP-like experiments are analyzed. The model used is the atmospheric component (Global Forecast System) of version 2 of the Climate Forecast System developed at the National

Centers for Environmental Prediction (NCEP; Saha et al. 2014). The model has a horizontal resolution of T126 (~105 km) and 64 vertical levels. The model is forced by the observed time-varying global monthly SSTs and sea ice. The SST and sea ice dataset are from the Hadley Centre Sea Ice and SST (HadISST) datasets for 1957-2008 (Rayner et al. 2006) and the Optimum Interpolation SST version 2 (OISSTv2) afterward (Reynolds et al. 2002). The integrations are from January 1957 to December 2018 and have 18 ensemble members with slightly different atmospheric initial conditions (Hu et al. 2017a).

In addition, the monthly SSTs from the Extended Reconstructed SST Version 5 (ERSSTv5; Huang et al. 2017) with a 2°x2° horizontal resolution are analyzed. ERSSTv5 SST has been used at NCEP/CPC in real-time monitoring ENSO evolution and defining ENSO event (https://origin.cpc.ncep.noaa.gov/products/analysis_monitoring/ensostuff/ONI_v5.php). Using ERSSTv5 SST anomalies with respect to climatology of January 1981-December 2010, following indices are defined:

Niño3.4 index: SSTA (5°S-5°N, 170°W-120°W) (Barnston et al. (1997);

ENSO-Modoki index: SSTA (10°S-10°N, 165°E-140°W) - [SSTA (15°S-5°N, 110°W-170°W) + SSTA (10°S-20°N, 125°E-145°E)]/2.0 (Ashok et al. 2007);

Cold tongue index: SSTA (5°S-5°N, 150°W-90°W)-0.4*SSTA (5°S-5°N, 160°E-150°W) (Ren and Jin 2011);

Warm pool index: SSTA (5°S-5°N, 160°E-150°W)-0.4*SSTA (5°S-5°N, 150°W-90°W) (Ren and Jin 2011);

Atlantic Niño (ATL3) index: SSTA (3°S-3°N, 0°-20°W) (Zebiak 1993);

Indian Ocean Dipole (IOD) index: SSTA (10°S-10°N, 50°E-70°E)-SSTA (10°S-0°, 90°E-110°E) (Saji et al. 1999).

Indian Ocean Basin mode (IOB) index: SSTA(20°S–20°N, 40°–110°E) (Yang et al. 2009).

These indices are used to examine the connections of global land precipitation variability with the SST variability in individual tropical ocean basins. To be a benchmark of the robustness of the SST-precipitation connection, we also calculate the correlations between the global land precipitation anomalies and a random time series with uniform distribution and in range of 0~1.0.

The corresponding observed precipitation is the monthly mean reconstructed precipitation analysis (Chen et al. 2002). It was developed by the optimal interpolation of gauge observations over the land only and covers the period from January 1948 to December 2018 on a 1° × 1° spatial resolution. This precipitation product has been widely used in the climate community both in operation and research (e.g., Li et al. 2016; Sun et al. 2018).

3. Spatial variations in SST-precipitation relationship

In the AMIP simulations, the externally specified forcing is the observed SST, and hence, is the source of predictability (and prediction skill) in precipitation variability. To quantify the influence of SST on precipitation, the correlation of precipitation anomalies (relative to 1981-2010 climatology) between the ensemble mean of the AMIP simulations and the observations is calculated and shown in Fig. 1a. The correlations are generally positive but are small with a maximum of 0.3~0.4 in the tropical North Africa along 15°N and northeastern Brazil (Kayano et al. 1988), implying only a moderate influence of SST anomalies on the precipitation variation (Fig. 1a). Here, we should note that, as expected, the correlations increase with the increase of ensemble size in the regions between 40°S and 40°N (Fig. 2). The increasing of correlation is more noticeable with the increasing of ensemble size from 1 to 10, and becomes less obvious while ensemble size larger than 10. That is generally consistent with previous work, such as, Brankovic and Palmer

(1997), Kumar and Hoerling (2000), Kumar et al. (2001), Kumar and Chen (2015). For the mid- and high- latitudes, the impact of the ensemble size on the correlation is still visible for some latitude zones with positive correlation, but the impact is undistinguishable when the correlations are near zero or negative and is consistent with results of Kumar and Hoerling (2000). They argued that there is no influence of ensemble size on skill when correlation is close to zero (see their Fig. 3).

It is feasible that overall low correlation might partially be caused by the design of AMIP simulations that cannot incorporate coupled air-sea interactions (Wu and Kirtman, 2005; Wang et al. 2005; Zhu and Shukla 2013). In fact, the amplitudes of correlation are comparable to other studies that utilized coupled prediction framework (e.g., see Fig. 3 in Jia et al. 2015), therefore the overall influence of coupled air-sea interactions may be small. The largest positive correlations are located in tropical Northern Africa, southern Africa, central Asia, western and eastern Australia, the southern part of North America, and the northeastern part of South America. These regions with higher correlation have been noted in previous works, such as Ropelewski and Halpert (1987), Yulaeva and Wallace (1994), and the National Research Council (2010). For the mid-high latitudes of the Northern Hemisphere (NH), both small positive and negative correlations are present, suggesting a smaller role of SST in influencing precipitation variability in these regions compared with that in the lower latitudes.

To assess the influence of model biases in the model simulations, an estimate of skill based on the assumption of a perfect model (SPM) is also computed. SPM is defined here as the averaged correlation between each individual member and the ensemble mean of the other 17 ensemble members. It has been shown that depending on the signal-to-noise ratio, SPM can also underestimate of the inherent potential skill (and predictability) in some regions due to model biases (Kumar et al. 2014; Scaife and Smith 2018; Baker et al. 2018; Dunstone et al. 2018). All SPMs are positive, however, are smaller than 0.5 (Fig. 1b). Overall spatial distribution patterns of the skill are similar between Fig. 1a and 1b, but the SPM in Fig. 1b is clearly larger than the correlations in Fig. 1a. The differences between Fig. 1a and 1b are noticeable in the subtropical southern Africa, Indian peninsular, southeastern Asia, northern and central parts of Australia, tropical North America, and the western part of South America. One of the possibilities of having large differences in these regions might be associated with large biases in the model, either in the amplitude of internal variability and/or the signal associated with SSTs, a topic that will require further investigation.

High (low) SPM is linked to large (small) signal-to-noise ratio (SNR) (Fig. 1c). Here, the signal is referred to as the standard deviation of the ensemble mean (based on 18 members), and the noise is defined as the standard deviation of the spread of the individual member from the ensemble mean (Kumar et al. 2017). In a perfect model scenario, large (small) SNR is linked to the expected high (low) predictability (Kumar and Hoerling 2000; Kumar et al. 2017). Except for some tropical regions, SNR is mostly smaller than 0.5, indicating a substantial role of the atmospheric internal variability and the fact that the internal variability may be more important than the signal associated with remote and/or local SST forcing in determining the precipitation variability over the land. In fact, the low predictability seems largely a common and inherent feature of climate variability over the mid-high latitude land or oceans (Davis 1976; Madden 1976; Hu et al. 2011, 2017a; Liang et al. 2019). In mid-latitude variability is dominated by atmospheric internal variability and has a smaller influence from external and/or remote boundary forcings, such as SST in the tropical oceans (Kumar et al. 2013; Kumar and Chen 2017; Deser et al. 2018).

The relatively high correlations in Fig. 1a and 1b and large values in Fig. 1c are mostly associated with the influence of SST variability in the central and eastern tropical Pacific Ocean and the tropical Indian Ocean (Fig. 3a-d, g). Correlations of precipitation anomaly with the Niño3.4 index are relatively high positive in the central Asia, southern United States, eastern tropical Africa, and southeastern South America, and relatively high negative in southern Africa, eastern Australia, and tropical South America. These regions also correspond to the relatively high correlations shown in Fig. 1a, large SPM in Fig. 1b and large SNR in Fig. 1c, suggesting the robust impact of SST anomaly on the precipitation variations in these regions. The correlations using different ENSO indices (Niño3.4, ENSO-Modoki, cold tongue, and warm pool indices, Fig. 3a-d) display a similar spatial pattern, although the overall correlations are slightly higher with the Niño3.4 index (Fig. 4).

For the impact of SST anomalies in the entire tropical Indian Ocean (represented by IOB index, Fig. 3g), the large positive correlations present over the U. S. and high latitudes of North America, Greenland, mid-latitudes of Asia, southeastern South America, and tropical Africa, while the negative ones in Australia, South Africa, and tropical South America. For the IOD index (Fig. 3f), the overall corrections are smaller than those associated with the IOB index. The positive correlations are in the eastern tropical Africa, and negative correlations in the Maritime Continent (Fig. 3f). In addition to the tropical Pacific and Indian Oceans, SSTs in the tropical Atlantic Ocean also affect some regional precipitation variations. For the ATL3 index, the relatively high correlations are in the tropical Africa and Southern America (Fig. 3e). Positive correlations present in the sub-polar north Atlantic region, which might be associated with the long-term trend of sea-ice change and deserves further investigation.

All these regions with relatively high positive and negative correlations shown in Fig. 3e-g may contribute to the relatively large values of correlation in these regions shown in Fig. 1, implying remoting influence of the tropical ocean SST anomalies on the precipitation variations over the global land. The impact of the SST anomalies in these various key regions (Fig. 3) on the precipitation is realized through various teleconnections. For example, the Niño indices associated SST anomalies in the central and eastern tropical Pacific affect the precipitation anomalies in the North American continent mainly through a Pacific–North American -like teleconnection pattern, which alters the intensity and location of the mid-latitude jet stream (e.g., Wallace and Gutzler 1981; Li et al. 2019). For the impact of ENSO on the eastern Asian climate, it is mainly through a Pacific-Japan teleconnection (e.g., Nitta 1987; Nitta and Hu 1996; Wang et al. 2000; Wu et al. 2003; Kosaka et al. 2012). The warm (cold) events in the eastern Pacific cause the weak (strong) East Asian winter monsoons through generating an anomalous lower-tropospheric anticyclone (cyclone) located in the western North Pacific. The connections of the precipitation in the northeastern Brazil and Indian summer monsoon with El Niño are mainly attributed to large-scale changes in a longitudinal displacement in the Walker circulation (e.g., Kayano et al. 1988; Ju and Slingo 1995).

Nevertheless, it should be pointed out that SST anomalies in the different ocean basins are also interconnected, especially for the tropical oceans. For instance, SST variability in the tropical Indian and Atlantic Oceans are partially a response to ENSO (Cai et al. 2019; Wang 2019). Compared with amplitudes of the correlations with the various SST indices (Fig. 3a-g), the correlations between the precipitation and a random time series are smaller and less significant (Fig. 3h), implying contributions of SST variability in all these ocean basins to the precipitation variation over the global land. To measure the mean global impact of each of these indices, Fig. 4

show the global averaged values of absolute correlations of Fig. 3. The value is the largest for the Niño3.4 index, the second largest for the IOB index, and the lowest for the IOD index. The values are comparable for the ENSO-Modoki and ATL3 indices. All the values for the various SST indices are larger than that for the random time series, implying that SST anomalies in all the tropical oceans do have an impact on precipitation variability over the global land as a whole. These features shown in Figs. 3 and 4 are further confirmed in Fig. 5, which shows a measure of the integrated influence of SST anomaly (over different ocean regions) on precipitation variability over the land. To get this measure, at each grid point in the ocean, the percentage of land grid points having significant correlations (at 95% significant level) with SST is shown. For instance, if at an ocean grid point the value is 10, it means that for 10% grid points over land precipitation has significant (either positive or negative) correlations (at 95% significant level) with SST anomaly at the ocean grid point.

The largest values are located in the central and eastern tropical Pacific and tropical Indian Oceans, the moderate values are located in the tropical western Pacific Ocean, small values in the tropical Atlantic Ocean (Fig. 5). It is interesting to note that the maximum values in the central tropical Pacific Ocean and in the central tropical Indian Ocean are comparable. Also, the values are smaller in the extratropics compared to the tropics, probably due to a larger influence of internal dynamical processes and larger uncertainties of SST in the extratropical oceans (Huang et al. 2018). These results suggest that SST anomalies in different oceans have different effectiveness in influencing precipitation variability over different land regions. The SST anomalies in the tropical Pacific associated with ENSO and in the central tropical Indian Ocean have the largest influence on precipitation variability over the global land, and the western Pacific, as well as the tropical Atlantic Ocean, which plays a secondary role. In addition to the SST indices used in Figs.

3 and 4, which mainly reflects SST variability in the seasonal-interannual time scales, some climate modes or indices with long-term time scales such as Pacific Decadal Oscillation (PDO), Atlantic Meridional Overturning Circulation (AMOC), and Atlantic Multidecadal Oscillation (AMO) may also play a role in the connection between SST and precipitation over the global land.

4. Temporal fluctuations

In addition to the spatial variations of precipitation response to SST anomaly, there are also temporal fluctuations in the response. One prominent variation is the seasonal cycle in the precipitation response to SSTs. For the seasonal cycle of the pattern correlation in each hemisphere (Fig. 6), which is defined as correlations in each individual month and hemisphere, the pattern correlation is larger in boreal winter than in boreal summer in NH. While in the Southern Hemisphere (SH), the seasonal dependence is not as distinct as in NH, and the pattern correlations are relatively larger in April-June, and September-November. This is consistent with previous works, such as Davey et al. (2014). Such seasonal dependence may be associated with the seasonal cycle of the tropical SST associated with ENSO and its lagged impact. Climatologically, compared to boreal summer, SST variability in the eastern and central tropical Pacific is larger due to the fact that ENSO peaks in boreal winter. Larger variability corresponds to a higher prediction skill and a larger impact on extratropical climate (National Research Council 2010; Hu et al. 2019). For SH, the seasonal variation of the impact may be due to the influence of SST anomaly in the Indian Ocean, which is partially linked to the lagged impact of ENSO (Shinoda et al. 2004).

In addition to the seasonal variation, the evolution of global pattern correlation also experiences interdecadal variations (Fig. 7). The pattern correlation is lower during 1957-1980 and 2000-2018, and higher in between, which has some similarity with the standard deviation of the

Niño3.4 index (dashed line in Fig. 7). On average, the higher (lower) correlations correspond to larger (smaller) variability of ENSO (Fig. 8). The decline of the pattern correlations since 1999/2000 is consistent with the decrease of the forecast skill of ENSO noted in previous works (Wang et al. 2010; Barnston et al. 2012). Previous works show that the decline is associated with the interdecadal change of ENSO properties, including suppression of variability and increase of frequencies (McPhaden 2012; Hu et al. 2013, 2016, 2017b, 2017c; Hu and Fedorov 2018). Nevertheless, interdecadal variations in the North Pacific and the Atlantic Ocean (such as PDO, AMOC, and AMO) may also play a role in the interdecadal variation of the correlations shown in Figs. 7 and 8. That deserves further investigation.

As a predominant factor affecting climate variability and predictability (National Research Council 2010), ENSO is linked to the variability of pattern correlation. Statistically, stronger ENSO year has a larger pattern correlation (Fig. 9). To check the symmetric impact of the cold and warm phases of ENSO on precipitation over the global land, the correlations between the pattern correlations of the AMIP simulation and the Niño3.4 index shown in Fig. 9 are computed separately for positive and negative Niño3.4 index. Specifically, for positive Niño3.4 index, the correlation with the pattern correlation is 0.27, while it is -0.29 for negative Niño3.4 index. The comparable correlation amplitudes for positive and negative Niño3.4 index may be an indication that global SST anomalies associated with an ENSO cycle have an overall comparable influence on precipitation variability over the global land as a whole. On the other hand, the profound spread shown in Fig. 9 implies large uncertainty of the connection between SST anomalies in ENSO years and precipitation variation over the global land as well as the impact of other factors than SST.

5. Summary and discussion

In this work, we quantitatively examined the role of SST on the variability and predictability of precipitation over the land by analyzing AMIP simulations forced by observed historical SST in 1958-2018. It was noted that the correlations of the monthly mean precipitation anomalies between the ensemble mean of the AMIP simulations and the observations were dominated by positive values with maximum values around 0.3~0.4. The integrated importance of SST in various ocean regions to precipitation variability over the global land is identified. The SST forcing for the global land precipitation is mainly located in the tropical Pacific Ocean that primarily associated with ENSO (e.g., Quan et al. 2006; Scaife et al. 2018), as well as in the tropical Indian Ocean, with some contribution from other ocean basins or modes, such as the western Pacific, Indian Ocean dipole and tropical Atlantic variabilities. Moreover, positive and negative SST anomalies associated with an ENSO cycle have an overall comparable influence on precipitation variability over the global land.

In addition to the spatial variations in precipitation response to SST, there are also temporal fluctuations. For the seasonal cycle of the pattern correlation, the correlation is larger in boreal winter than in boreal summer in NH, and relatively larger in April-June and September-November in SH. The global average of correlation also varies from decade to decade: it is lower during 1957-1980 and 2000-2018, and higher in between. Such interdecadal fluctuation of the pattern correlation is coherent with the interdecadal variation of ENSO intensity. For example, the decline of the pattern correlations since 1999/2000 could be associated with the suppression of variability and increase of frequencies of ENSO (McPhaden 2012; Hu et al. 2013, 2016, 2017b, 2017c; Hu and Fedorov 2018).

Considering the fact that SST anomaly is the major source of global climate variability and predictability at seasonal-interannual time scales (National Research Council 2010), the overall small correlations may imply inherently low predictability and low prediction skill for monthly mean precipitation variability over the global land as whole. As observed sea ice variations are used in the AMIP simulations, thus, predictability examined in this work may also partially be associated with sea ice variation.

Acknowledgments:

We appreciate the comments and suggestions of two reviewers as well as our colleagues Drs. Peitao Peng and Caihong Wen. The scientific results and conclusions, as well as any view or opinions expressed herein, are those of the authors and do not necessarily reflect the views of NWS, NOAA, or the Department of Commerce.

References

Ashok, K., S. K. Behera, S. A. Rao, H. Weng, and T. Yamagata, 2007: El Niño Modoki and its possible teleconnection. *J. Geophys. Res*., **112**, C11007. DOI: 10.1029/2006JC003798.

Baker, L. H., L. C. Shaffrey, R. T. Sutton, A. Weisheimer, and A. A. Scaife 2018: An intercomparison of skill and overconfidence/underconfidence of the wintertime North Atlantic Oscillation in multimodel seasonal forecasts. *Geophys. Res. Lett.,* **45**, 7808– 7817. DOI: 10.1029/2018GL078838.

Barnston, A. G., M. Chelliah and S.B. Goldenberg, 1997: Documentation of a highly ENSO-related SST region in the equatorial Pacific. *Atmosphere-Ocean*, **35,** 367-383. DOI: 10.1080/07055900.1997.9649597.

Barnston, A. G., M. K. Tippett, M. L. L'Heureux, S. Li, and D. G. DeWitt, 2012: Skill of real-time seasonal ENSO model predictions during 2002-2011 — Is our capability increasing? *Bull. Amer. Meteor. Soc.,* **93 (5),** 631-651. DOI: 10.1175/BAMS-D-11-00111.1.

Brankovic, C., and T. N. Palmer, 1997: Atmospheric seasonal predictability and estimates of ensemble size. *Mon. Wea. Rev*., **125**, 859–874. DOI: 10.1175/1520-0493(1997)125<0859:ASPAEO>2.0.CO;2.

Cai, W, et al., 2019: Pantropical climate interactions. Science, 363 (6430). DOI: 10.1126/science.aav4236.

Chen, M., P. Xie, J. E. Janowiak, and P. A. Arkin, 2002: Global land precipitation: A 50-yr monthly analysis based on gauge observations. *J. Hydrometeor*., **3**, 249–266. DOI: 10.1175/1525-7541(2002)003<0249:GLPAYM>2.0.CO;2.

Davey, M. K., A. Brookshaw, and S. Ineson, 2014: The probability of the impact of ENSO on precipitation and near-surface temperature. *Climate Risk Management*, **1**, 5-24. DOI: 10.1016/j.crm.2013.12.002

Davis, R. E., 1976: Predictability of sea surface temperature and sea level pressure anomalies over the North Pacific Ocean. *J. Phys. Oceanogr*., **6**, 249–266. DOI: 10.1175/1520-0485(1976)006<0249:POSSTA>2.0.CO;2.

Deser, C., I. R. Simpson, A. S. Phillips, and K. A. McKinnon, 2018: How well do we know ENSO's climate impacts over North America, and how do we evaluate models accordingly?. *J. Climate*, **31**, 4991–5014, https://doi.org/10.1175/JCLI-D-17-0783.1.

Dunstone, N., A. A. Scaife, C. MacLachlan, et al., 2018: Predictability of European winter 2016/2017. *Atmos Sci Lett.,* **19 (e868).** DOI: 10.1002/asl.868.

Goddard, L. and M. Dilley, 2005: El Niño: Catastrophe or opportunity. *J. Climate*, **18**, 651–665. DOI: 10.1175/JCLI-3277.1.

Hu, S. and A. V. Fedorov, 2018: Cross-equatorial winds control El Niño diversity and change. *Nature Climate Change*, **8**, 798-802. DOI: 10.1038/s41558-018-0248-0.

Hu, Z.-Z., A. Kumar, B. Huang, Y. Xue, W. Wang, and B. Jha, 2011: Persistent atmospheric and oceanic anomalies in the North Atlantic from Summer 2009 to Summer 2010. *J. Climate,* **24 (22),** 5812-5830. DOI: 10.1175/2011JCLI4213.1.

Hu, Z.-Z., A. Kumar, H.-L. Ren, H. Wang, M. L'Heureux, and F.-F. Jin, 2013: Weakened interannual variability in the tropical Pacific Ocean after 2000. *J. Climate*, **26 (8)**, 2601-2613. DOI: 10.1175/JCLI-D-12-00265.1.

Hu, Z.-Z., A. Kumar, and B. Huang, 2016: Spatial distribution and the interdecadal change of leading modes of heat budget of the mixed-layer in the tropical Pacific and the association with ENSO. *Climate Dyn.,* **46 (5-6),** 1753-1768. DOI: 10.1007/s00382-015-2672-4.

Hu, Z.-Z., A. Kumar, B. Jha, J. Zhu, and B. Huang, 2017a: Persistence and predictions of the remarkable warm anomaly in the northeastern Pacific Ocean during 2014-2016. *J. Climate,* **30 (2),** 689–702. DOI: 10.1175/JCLI-D-16-0348.1.

Hu, Z.-Z., A. Kumar, B. Huang, J. Zhu, and H.-L. Ren, 2017b: Interdecadal variations of ENSO around 1999/2000. *J. Meteor. Res*., **31 (1),** 73-81. DOI: 10.1007/s13351-017-6074-x.

Hu, Z.-Z., A. Kumar, J. Zhu, B. Huang, Y.-h. Tseng, and X. Wang, 2017c: On the shortening of the lead time of ocean warm water volume to ENSO SST since 2000. *Sci. Rep.,* **7,** 4294. DOI: 10.1038/s41598-017-04566-z.

Hu, Z.-Z., A. Kumar, J. Zhu, P. Peng, and B. Huang, 2019: On the challenge for ENSO cycle prediction: An example from NCEP Climate Forecast System version 2. *J. Climate*, **32 (1),** 183-194. DOI: 10.1175/JCLI-D-18-0285.1.

Huang, B., and Coauthors, 2017: Extended Reconstructed Sea Surface Temperature version 5 (ERSSTv5), Upgrades, validations, and intercomparisons. *J. Climate,* **30 (20),** 8179–8205. DOI: 10.1175/JCLI-D-16-0836.1.

Huang, B., W. Angel, T. Boyer, L. Cheng, G. Chepurin, E. Freeman, C. Liu, and H. Zhang, 2018: Evaluating SST Analyses with Independent Ocean Profile Observations. J. Climate, **31**, 5015–5030. DOI: 10.1175/JCLI-D-17-0824.1.

Jia, L., et al., 2015: Improved Seasonal Prediction of Temperature and Precipitation over Land in a High-Resolution GFDL Climate Model. *J. Climate*, **28**, 2044–2062. DOI: 10.1175/JCLI-D-14-00112.1.

Ju, J., and J. M. Slingo, 1995: The Asian summer monsoon and ENSO. *Q. J. R. Meteor. Soc.*, **121**, 1133–1168.

Kayano, M. T., V. B. Rao, and A. D. Moura, 1988: Tropical circulations and the associated rainfall anomalies during two contrasting years. *J. Climatol.,* **8**, 477–488.

Kosaka, Y., J. S. Chowdary, S.-P. Xie, Y.-M. Min, and J.-Y. Lee, 2012: Limitations of seasonal predictability for summer climate over East Asia and the Northwestern Pacific. *J. Climate*, **25**, 7574-7589. DOI: 10.1175/JCLI-D-12-00009.1.

Kumar, A., and M. P. Hoerling, 2000: Analysis of a conceptual model of seasonal climate variability and implications for seasonal prediction. *Bull. Am. Meteor. Soc.,* **81**, 255–264. DOI: 10.1175/1520-0477(2000)081<0255:AOACMO>2.3.CO;2.

Kumar, A., A. G. Barnston, and M. P. Hoerling, 2001: Seasonal predictions, probabilistic verifications, and ensemble size. *J. Climate*, **14**, 1671–1676. DOI: 10.1175/1520-0442(2001)014<1671:SPPVAE>2.0.CO;2.

Kumar A., H. Wang, W. Wang, Y. Xue, and Z.-Z. Hu, 2013: Does knowing the oceanic PDO phase help predict the atmospheric anomalies in subsequent months? *J. Climate*, **26 (4),** 1268-1285. DOI: 10.1175/JCLI-D-12-00057.1.

Kumar, A., P. Peng, and M. Chen, 2014: Is there a relationship between potential and actual kill? *Mon. Wea. Rev.,* **142**, 2220-2227. DOI: 10.1175/MWR-D-13-00287.1.

Kumar, A. and M. Chen, 2015: Inherent predictability, requirements on the ensemble size, and complementarit.y. *Mon. Wea. Rev.,* **143**, 3192–3203. DOI: 10.1175/MWR-D-15-0022.1.

Kumar, A. and M. Chen, 2017: What is the variability in US west coast winter precipitation during strong El Niño events? *Climate Dyn.,* **49 (7–8)**, 2789–2802. DOI: 10.1007/s00382-016-3485-9.

Kumar, A., Z.-Z. Hu, B. Jha, and P. Peng, 2017: Estimating ENSO predictability: based on multi-model hindcasts. *Climate Dyn.,* **48 (1-2)**, 39-51. DOI: 10.1007/s00382-016-3060-4.

Li, X., Z.-Z. Hu, X. Jiang, Y. Li, Z. Gao, S. Yang, J. Zhu, and B. Jha, 2016: Trend and seasonality of land precipitation in observations and CMIP5 model simulations. *Int. J. Climatol.*, **36 (11),** 3781-3793. DOI: 10.1002/joc.4592.

Li, X., Z.-Z. Hu, P. Liang, and J. Zhu, 2019: Contrastive influence of ENSO and PNA on variability and predictability of North American winter precipitation. *J. Climate*, **32 (19),** 6271-6284. DOI: 10.1175/JCLI-D-19-0033.1.

Liang, P., Z.-Z. Hu, Y. Liu, X. Yuan, X. Li, and X. Jiang, 2019: Challenges in predicting and simulating summer rainfall in the eastern China. *Climate Dyn.,* **52 (3-4),** 2217-2233. DOI: 10.1007/s00382-018-4256-6.

Madden, R.A., 1976: Estimates of the natural variability of time-averaged sea-level pressure. *Mon. Wea. Rev*., **104**, 942–952. DOI: 10.1175/1520-0493(1976)104<0942:EOTNVO>2.0.CO;2.

McPhaden, M. J., 2012: A 21st century shift in the relationship between ENSO SST and warm water volume anomalies. *Geophys. Res. Lett.*, **39**, L09706. DOI: 10.1029/2012GL051826.

National Research Council, 2010: *Assessment of Intraseasonal to Interannual Climate Prediction and Predictability*, 192 PP., ISBN-10: 0-309-15183-X, the National Academies Press, Washington, D. C., USA.

Nitta, T., 1987: Convective activities in the tropical western Pacific and their impact on the Northern Hemisphere summer circulation. *J. Meteorol. Soc. Jpn*., **65**, 373–390.

Nitta, T. and Z.-Z. Hu, 1996: Summer climate variability in China and its association with 500 hPa height and tropical convection. *J. Meteor. Soc. Japan*, **74(4),** 425-445. DOI: 10.2151/jmsj1965.74.4_425.

O'Lenic, E. A., D. A. Unger, M. S. Halpert, and K. S. Pelman, 2008: Developments in operational long-range climate prediction at CPC. *Wea. Forecasting*, **23**, 496–515. DOI: 10.1175/2007WAF2007042.1.

Peng, P., A. Kumar, A. G. Barnston, and L. Goddard, 2000: Simulation skills of the SST-forced global climate variability of the NCEP-MRF9 and Scripps/MPI ECHAM3 models. *J. Climate*, **13**, 3657–3679. DOI: 10.1175/1520-0442(2000)013<3657:SSOTSF>2.0.CO;2.

Peng, P., A. Kumar, M. S. Halpert, and A. G. Barnston, 2012: An analysis of CPC's operational 0.5-month lead seasonal outlooks. *Wea. Forecasting*, **27,** 898–917. DOI: 10.1175/WAF-D-11-00143.1.

Peng, P., A. G. Barnston, and A. Kumar, 2013: A comparison of skill between two versions of the NCEP Climate Forecast System (CFS) and CPC's operational short-lead seasonal outlooks. *Wea. Forecasting*, **28**, 445–462. DOI:10.1175/WAF-D-12-00057.1.

Quan, X., M. Hoerling, J. Whitaker, G. Bates, and T. Xu, 2006: Diagnosing sources of U.S. seasonal forecast skill. *J. Climate*, **19**, 3279–3293. DOI: 10.1175/JCLI3789.1

Rayner, N., P. Brohan, D. Parker, C. Folland, J. Kennedy, M. Vanicek, T. Ansell, and S. Tett, 2006: Improved analyses of changes and uncertainties in sea surface temperature measured in situ since the mid-nineteenth century: The HadSST2 data set. *J. Climate*, **19(3),** 446–469. DOI: 10.1175/JCLI3637.1.

Ren, H.-L., and F.-F. Jin, 2011: Niño indices for two types of ENSO. *Geophys. Res. Lett*., **38**, L04704. DOI: 10.1029/2010GL046031.

Reynolds, R. W., N. A. Rayner, T. M. Smith, D. C. Stokes and W. Wang, 2002: An improved in situ and satellite SST analysis for climate. *J. Climate*, **15**, 1609-1625. DOI: 10.1175/1520-0442(2002)015<1609:AIISAS>2.0.CO;2.

Ropelewski, C. F. and M. Halpert, 1987: Global and regional scale precipitation patterns associated with the El Niño-Southern Oscillation. *Mon. Wea. Rev.,* **115**, 1606-1626. DOI: 10.1175/1520-0493(1987)115<1606:GARSPP>2.0.CO;2.

Saha, S., et al., 2014: The NCEP Climate Forecast System version 2. *J. Climate*, **27**, 2185–2208. DOI: 10.1175/JCLI-D-12-00823.1.

Saji, N. H., B. N. Goswami, P. N. Vinayachandran, and T. Yamagata. 1999: A dipole mode in the tropical Indian Ocean. *Nature,* **401**, 360–363. DOI: 10.1038/43854.

Sarachik, E. S. and M. A. Cane, 2010: *The El Niño-Southern Oscillation Phenomenon*. Cambridge University Press, London, 384 pp.

Scaife, A. A. and D. Smith, 2018: A signal-to-noise paradox in climate science. *npj Cli-mate and Atmospheric Science,* **1,** 28. DOI: 10.1038/s41612-018-0038-4.

Scaife, A. A., et al. 2018: Tropical rainfall predictions from multiple seasonal forecast systems. *Int J Climatol*., **39,** 974–988. DOI: 10.1002/joc.5855.

Shinoda, T., M.A. Alexander, and H.H. Hendon, 2004: Remote Response of the Indian Ocean to Interannual SST Variations in the Tropical Pacific. *J. Climate*, **17**, 362–372. DOI: 10.1175/1520-0442(2004)017<0362:RROTIO>2.0.CO;2.

Sun, Q., C. Miao, Q. Duan, H. Ashouri, S. Sorooshian, and K.-L. Hsu, 2018: A review of global precipitation datasets: data sources, estimation, and intercomparisons. *Geophs. Rev*., **56 (1),** 79-107. DOI: 10.1002/2017RG000574.

Wallace, J. M., and D. S. Gutzler, 1981: Teleconnections in the geopotential height field during the Northern Hemisphere winter. *Mon. Wea. Rev*., **109**, 784-812.

Wang, B., R. Wu, and X. Fu, 2000: Pacific–East Asian teleconnection: How does ENSO affect East Asian climate? *J. Climate,* **13**, 1517–1536. DOI: 10.1175/1520-0442(2000)013<1517:PEATHD>2.0.CO;2.

Wang, B., Q. Ding, X. Fu, I.-S. Kang, K. Jin, J. Shukla, and F. Doblas-Reyes, 2005: Fundamental challenges in simulation and prediction of summer monsoon rainfall. *Geophys. Res. Lett.*, **32 (15),** L15711. DOI: 10.1029/2005GL022734.

Wang, C., 2019: Three-ocean interactions and climate variability: a review and perspective. *Clim. Dyn*. DOI: 10.1007/s00382-019-04930-x.

Wu, R., Z.-Z. Hu, and B. P. Kirtman, 2003: Evolution of ENSO-related rainfall anomalies in East Asia. *J. Climate*, **16 (22),** 3742-3758. DOI: 10.1175/1520-0442(2003)016<3742:EOERAI>2.0.CO;2.

Wu, R. and B. P. Kirtman, 2005: Roles of Indian and Pacific Ocean air–sea coupling in tropical atmospheric variability. *Climate Dyn.*, 25 (2-3), 155-170. DOI: 10.1007/s00382-005-0003-x.

Wang, W., M. Chen, and A. Kumar, 2010: An assessment of the CFS real-time seasonal forecasts. *Wea. Forecasting*, **25**, 950-969. DOI: 10.1175/2010WAF2222345.1.

Yang, J., Q. Liu, Z. Liu, L. Wu, and F. Huang, 2009: Basin mode of Indian Ocean sea surface temperature and Northern Hemisphere circumglobal teleconnection. *Geophys. Res. Lett.,* **36,** L19705, doi:10.1029/2009GL039559.

Yeh, S.-W. et al., 2018: ENSO atmospheric teleconnections and their response to greenhouse gas forcing. *Rev. Geophys*., **56 (1),** 185-206. DOI: 10.1002/2017RG000568.

Yulaeva, E., and J. M. Wallace, 1994: The signature of ENSO in global temperature and precipitation fields derived from the Microwave Sounding Unit. *J. Climate*, **7**, 1719–1736. DOI: 10.1175/1520-0442(1994)007<1719:TSOEIG>2.0.CO;2.

Zebiak, S. E., 1993: Air–sea interaction in the equatorial Atlantic region. *J. Climate*, **6**, 1567–1586. DOI: 10.1175/1520-0442(1993)006<1567:AIITEA>2.0.CO;2.

Zhu, J. and J. Shukla, 2013: The role of air–sea coupling in seasonal prediction of Asia–Pacific summer monsoon rainfall. *J. Climate,* **26**, 5689–5697. DOI: 10.1175/JCLI-D-13-00190.1.

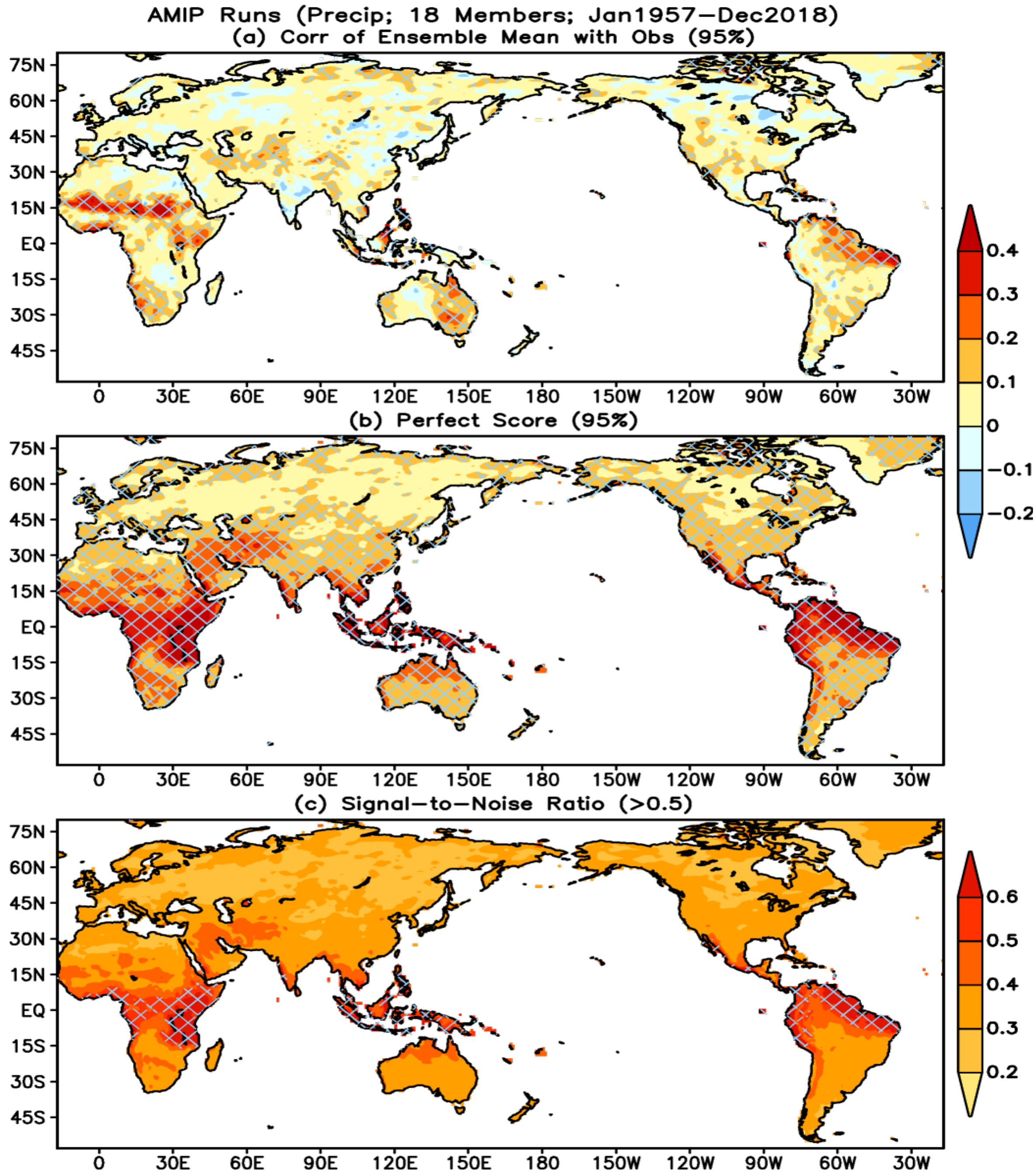

Fig. 1: (a) Correlations of monthly mean precipitation anomalies between observations and the ensemble means of the AMIP simulations with 18 ensemble members during January 1957-December 2018; (b) perfect model score, which is referred to as averaged correlation of each individual member with the ensemble mean of the other 17 members in the AMIP simulations; (c) signal-to-noise ratio (SNR) of the AMIP simulations. The hatched regions in (a, b) represent the correlations significant at 95% or higher confidence level using the T-test (correlation values larger than 0.1), and in (c) is for values larger than or equal to 0.5.

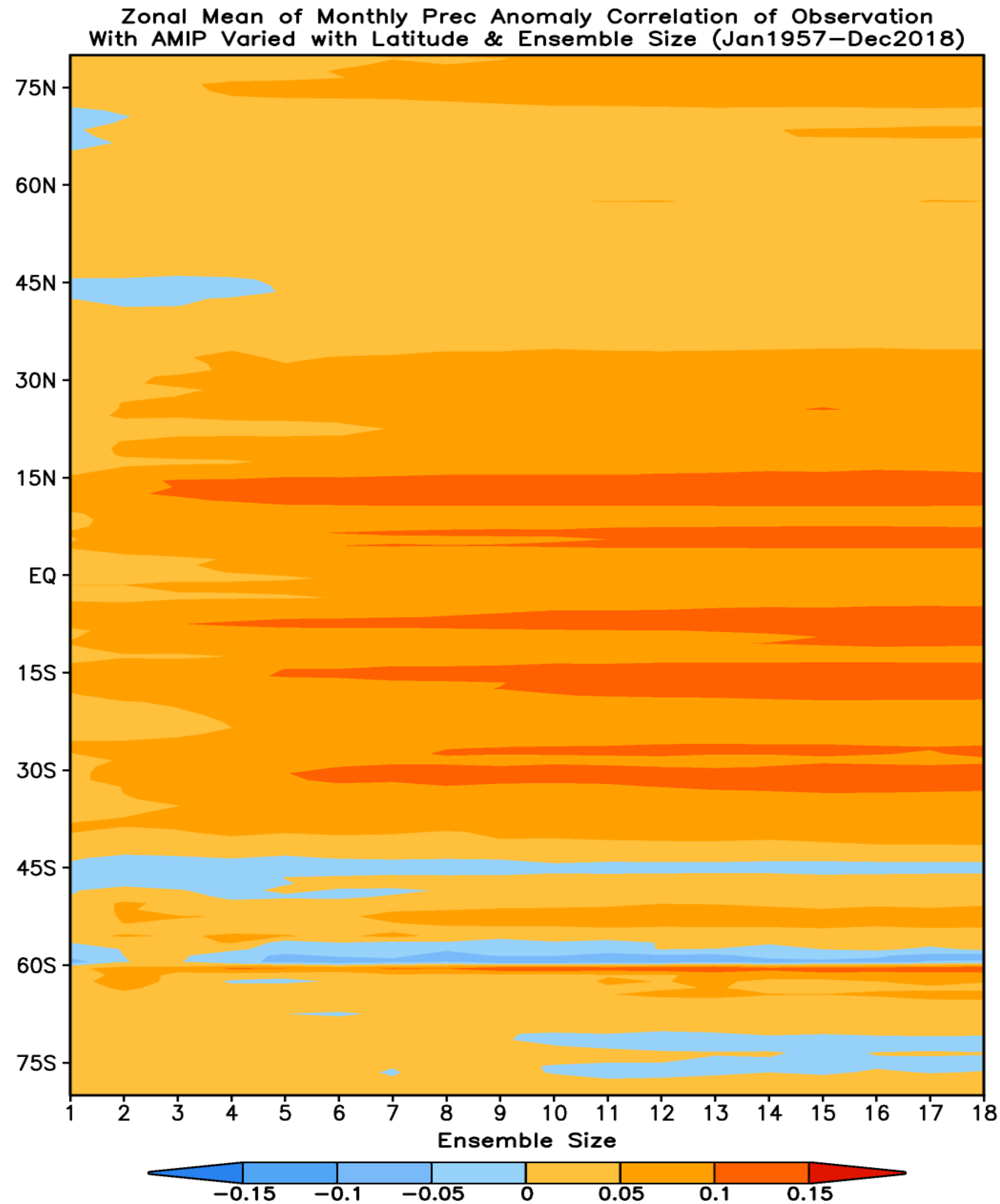

Fig. 2: Zonal mean correlations of the monthly mean precipitation anomalies between observations and the ensemble means of the AMIP simulations varied with latitude and ensemble size during January 1957-December 2018.

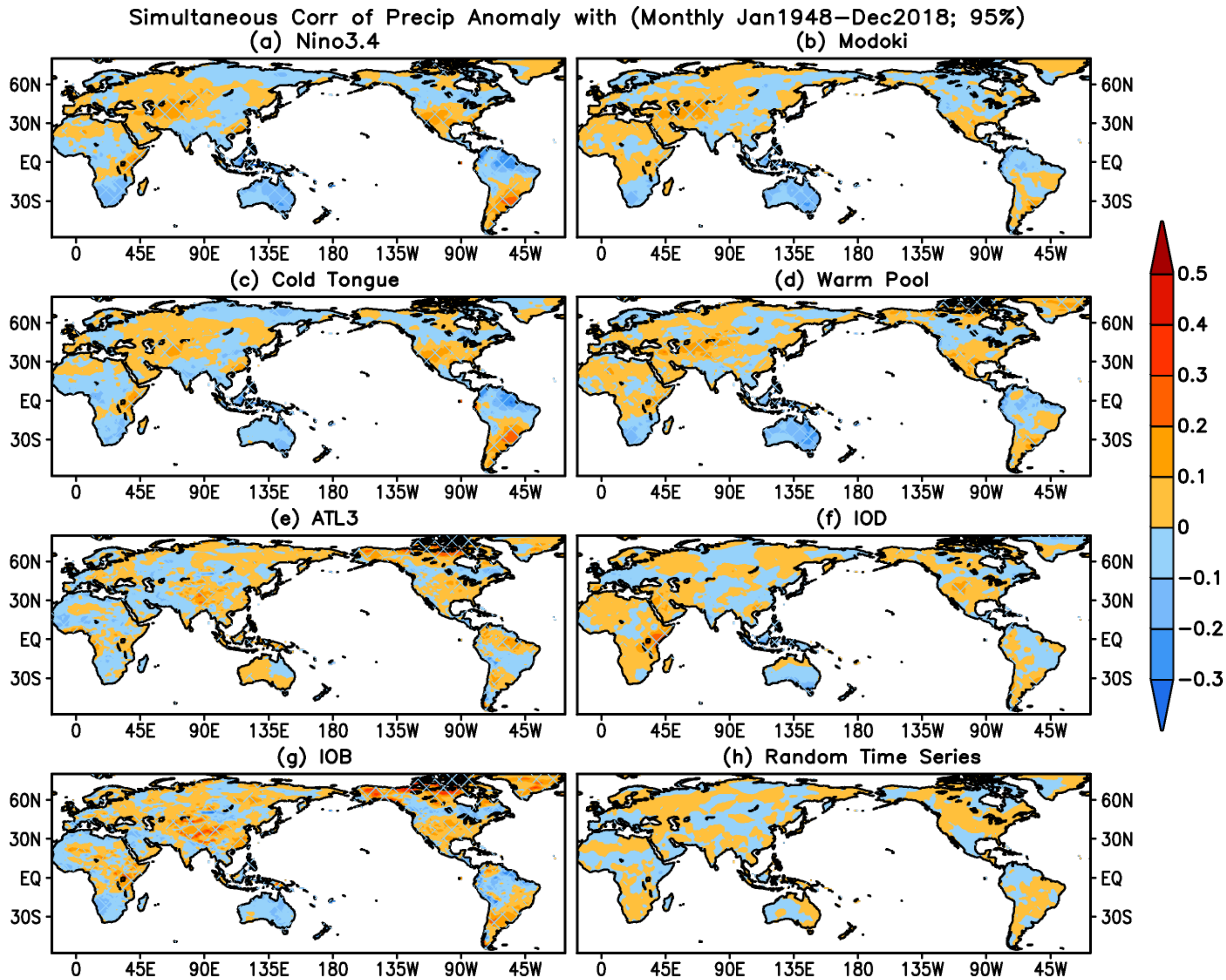

Fig. 3: Simultaneous correlations of observed monthly precipitation anomalies with (a) Niño3.4, (b) ENSO-Modoki, (c) warm pool, (d) cold tongue, (e) ATL3, (f) IOD, and (g) IOB indices during January 1948-December 2018 as well as (h) a random time series. Hatching represents significant correlations at the significance level of 95% using the T-test, corresponding to correlation values larger than 0.067. Shading interval is 0.1.

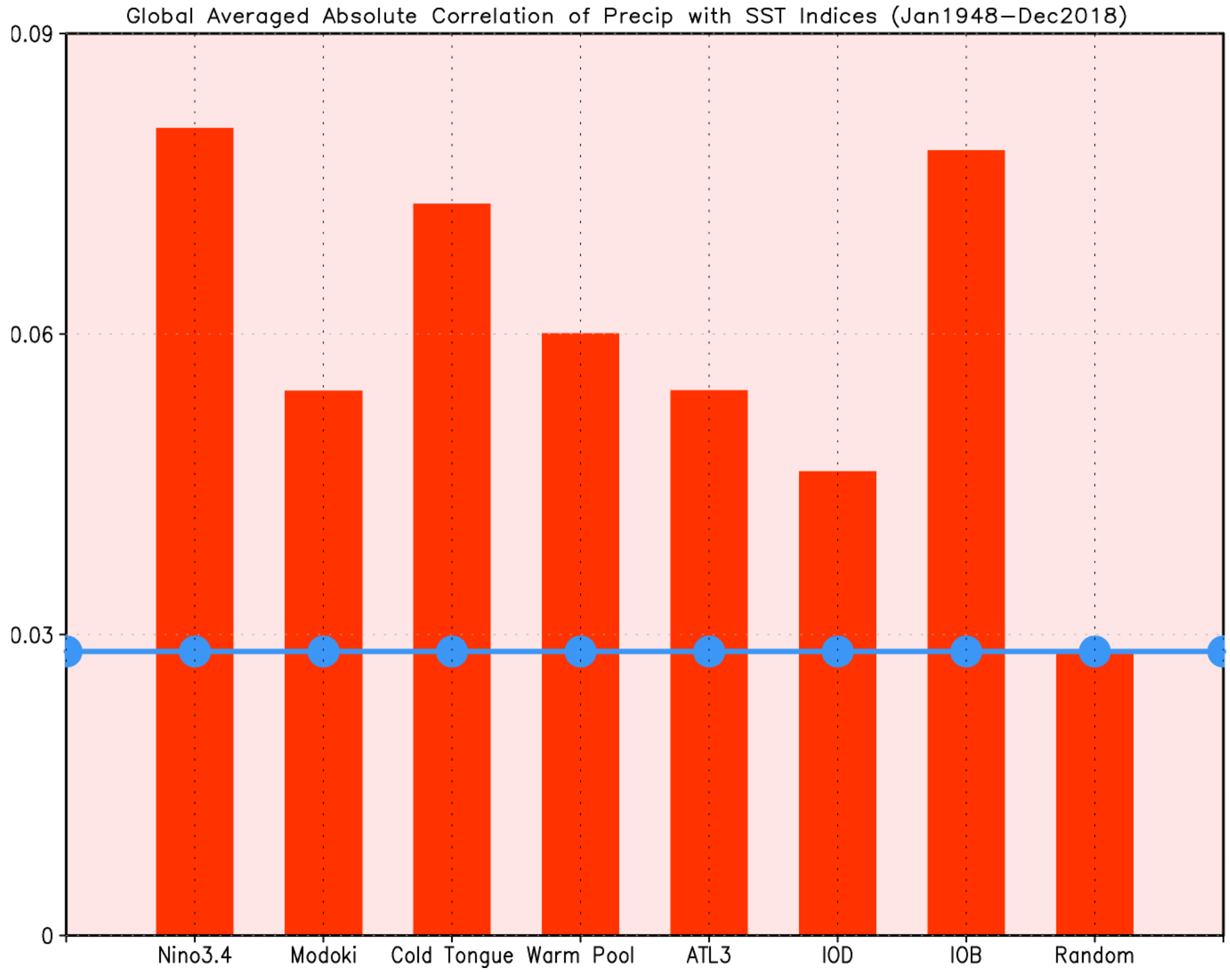

Fig. 4: Global averaged and area-weighted absolute correlations of observed monthly precipitation anomalies with Niño3.4, ENSO-Modoki, warm pool, cold tongue, ATL3, IOD, and IOB indices during January 1948-December 2018 as well as a random time series. The horizontal line represents the global averaged absolute correlations of observed monthly precipitation anomalies with the random time series.

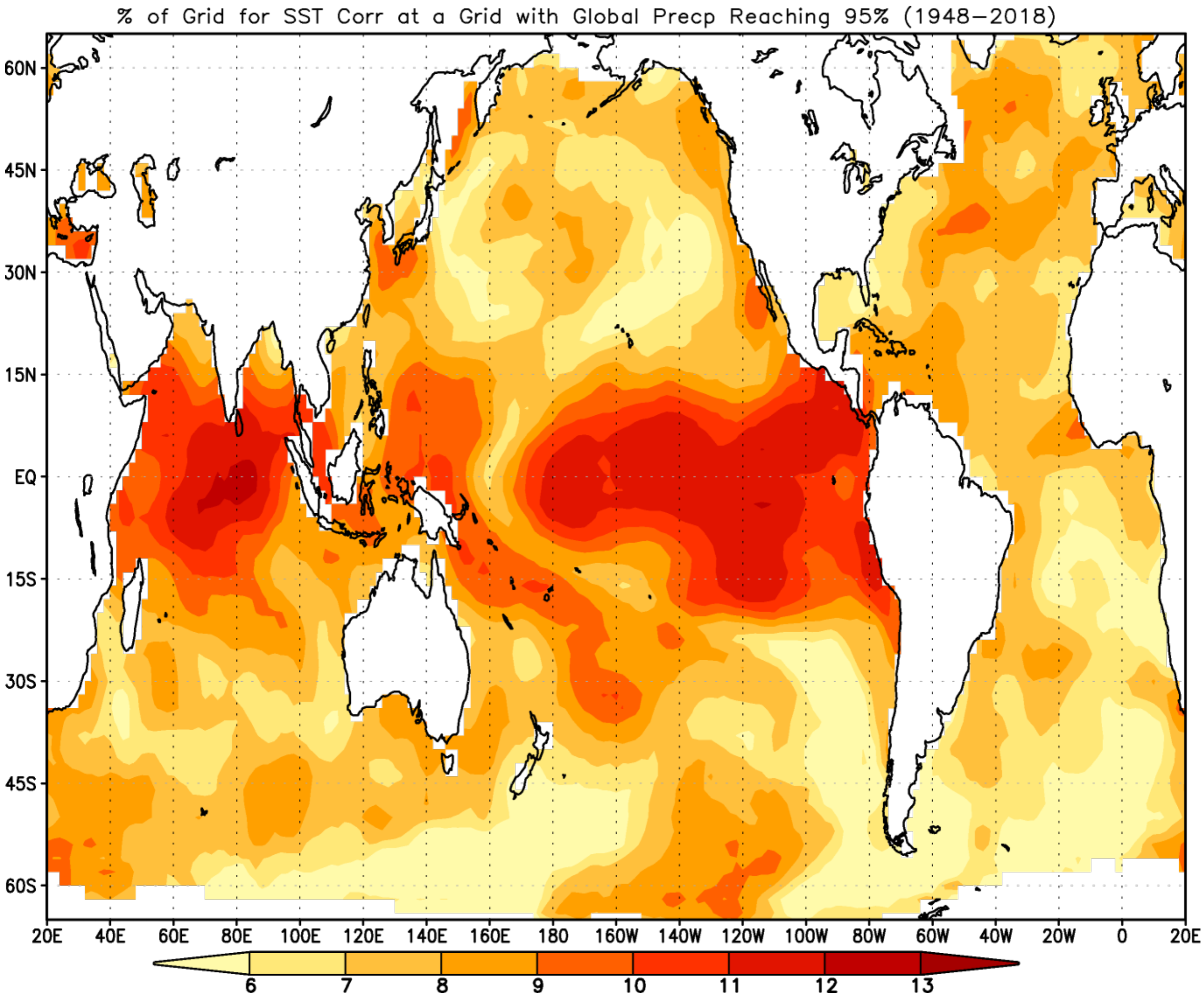

Fig. 5: Percentage of accumulated grid numbers for the correlation between observed SST anomaly at a grid and global precipitation anomalies which reaches 95% significance level using T-test, referred to total grid number of global land precipitation during January 1948-December 2018.

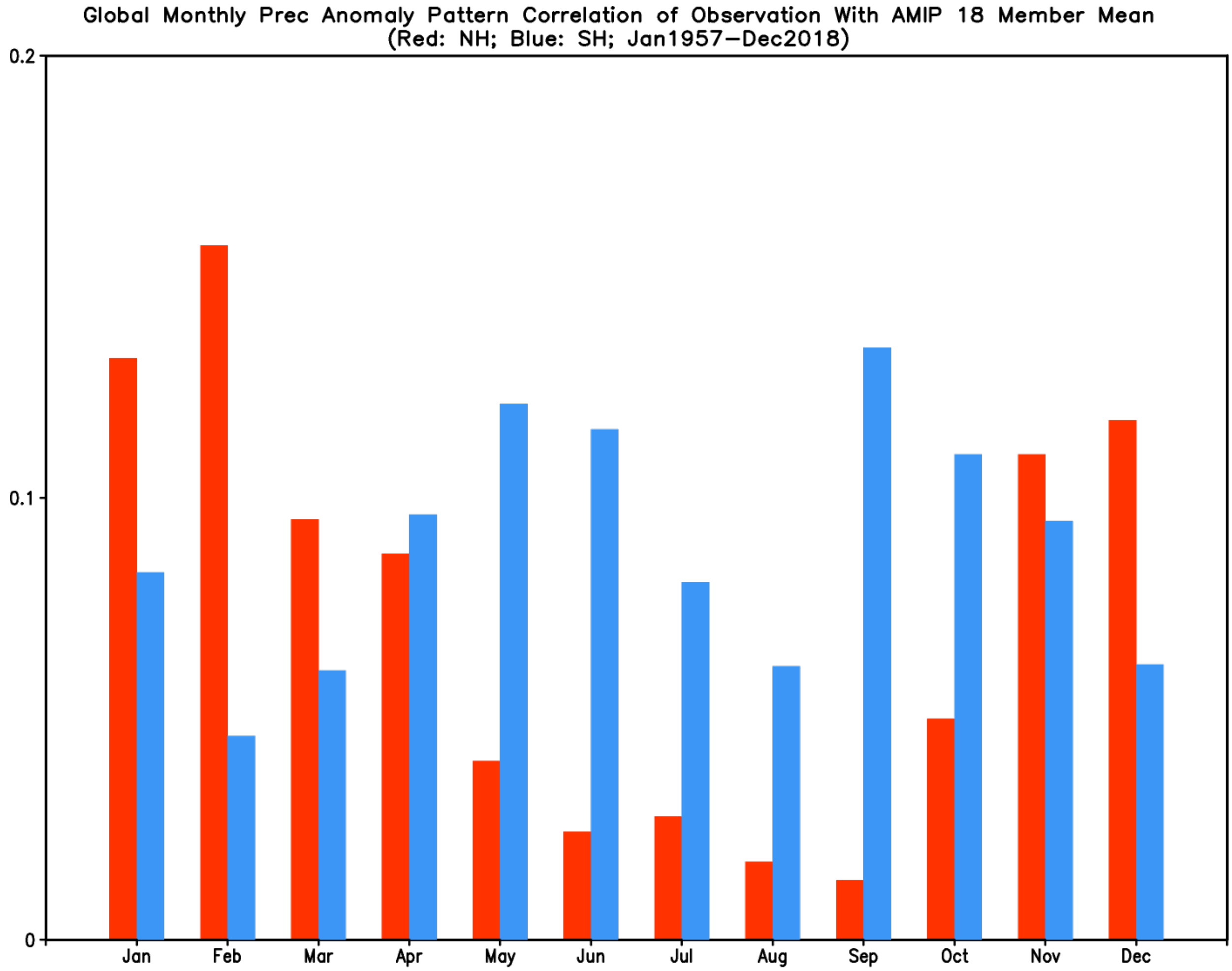

Fig. 6: Pattern correlations of monthly mean precipitation anomalies between observations and ensemble mean of AMIP simulations in each month for Northern Hemisphere (red bars) and Southern Hemisphere (blue bars) during January 1957-December 2018.

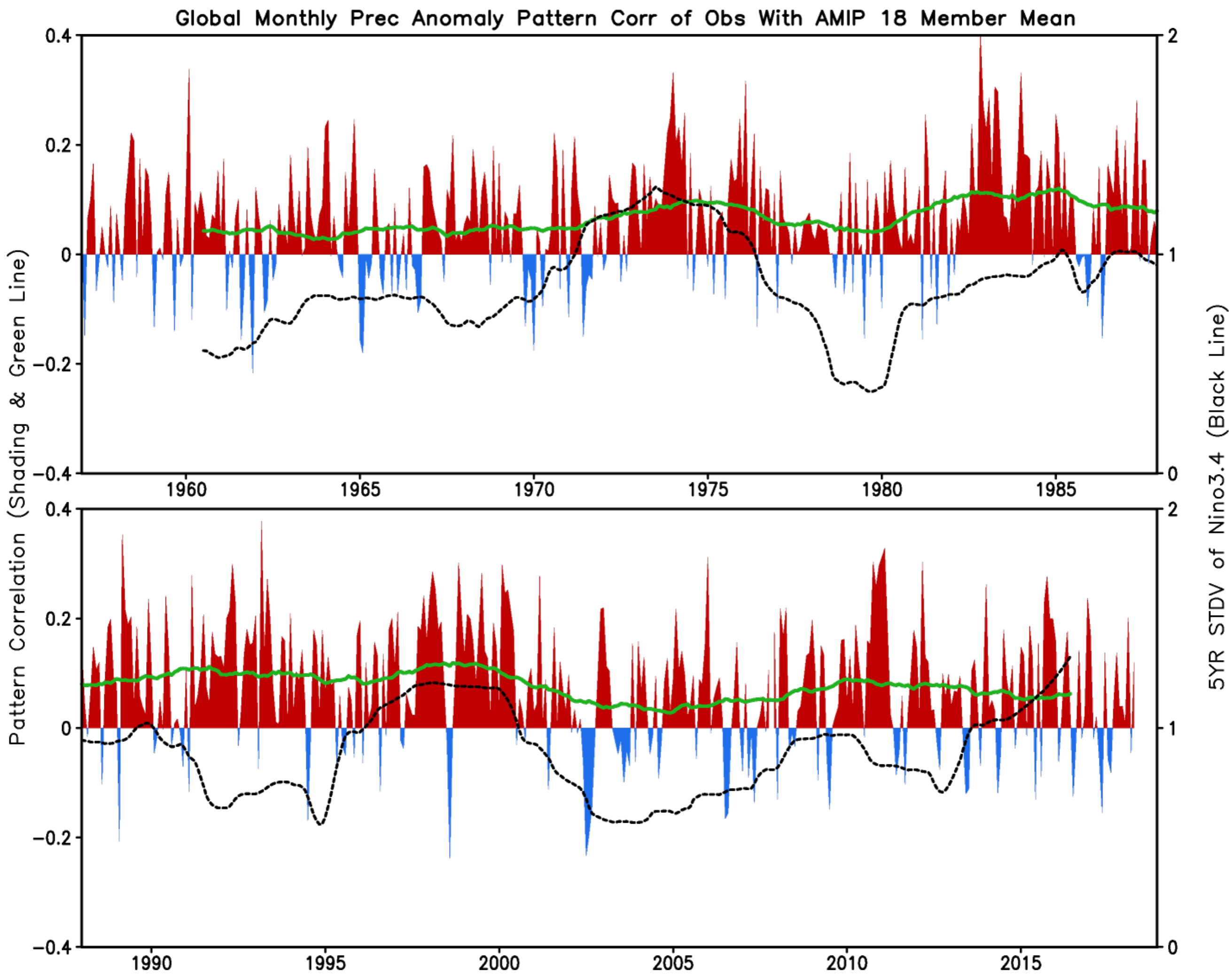

Fig. 7: Temporal evolution of pattern correlations of monthly mean precipitation anomalies between observations and ensemble mean of AMIP simulations in the globe (shading) and its 5-years running mean (green line) during January 1957-December 2018. Dashed line represents 5-years running mean of standard deviation of the Niño3.4 index.

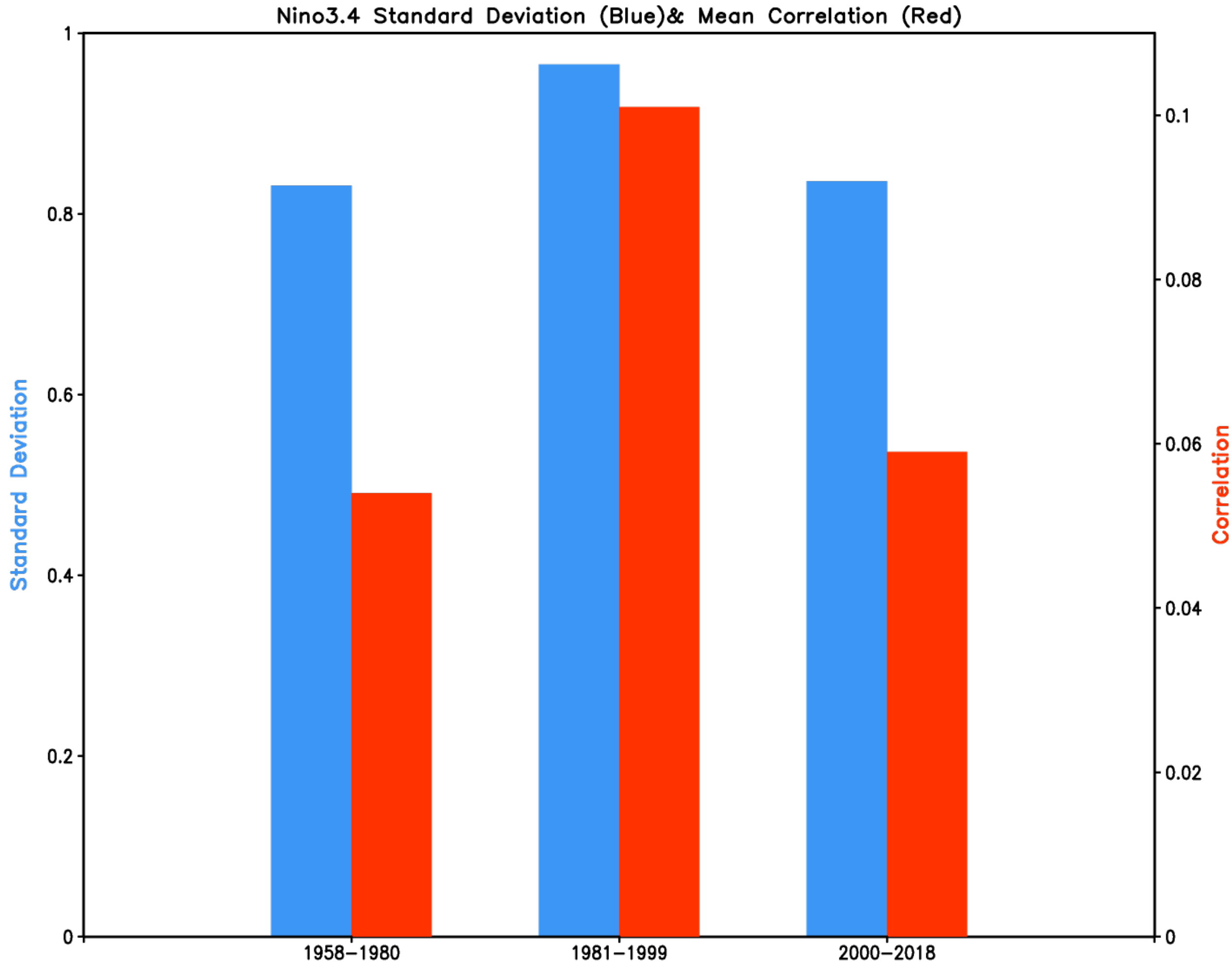

Fig. 8: Mean pattern correlations of monthly mean precipitation anomalies between observations and ensemble mean of AMIP simulations over the global land (red) and standard deviation of the Niño3.4 index (blue) averaged in January 1957-December 1980 (bar in left), January 1981-December 1999 (bar in the middle), and January 2000-December 2018 (bar in right).

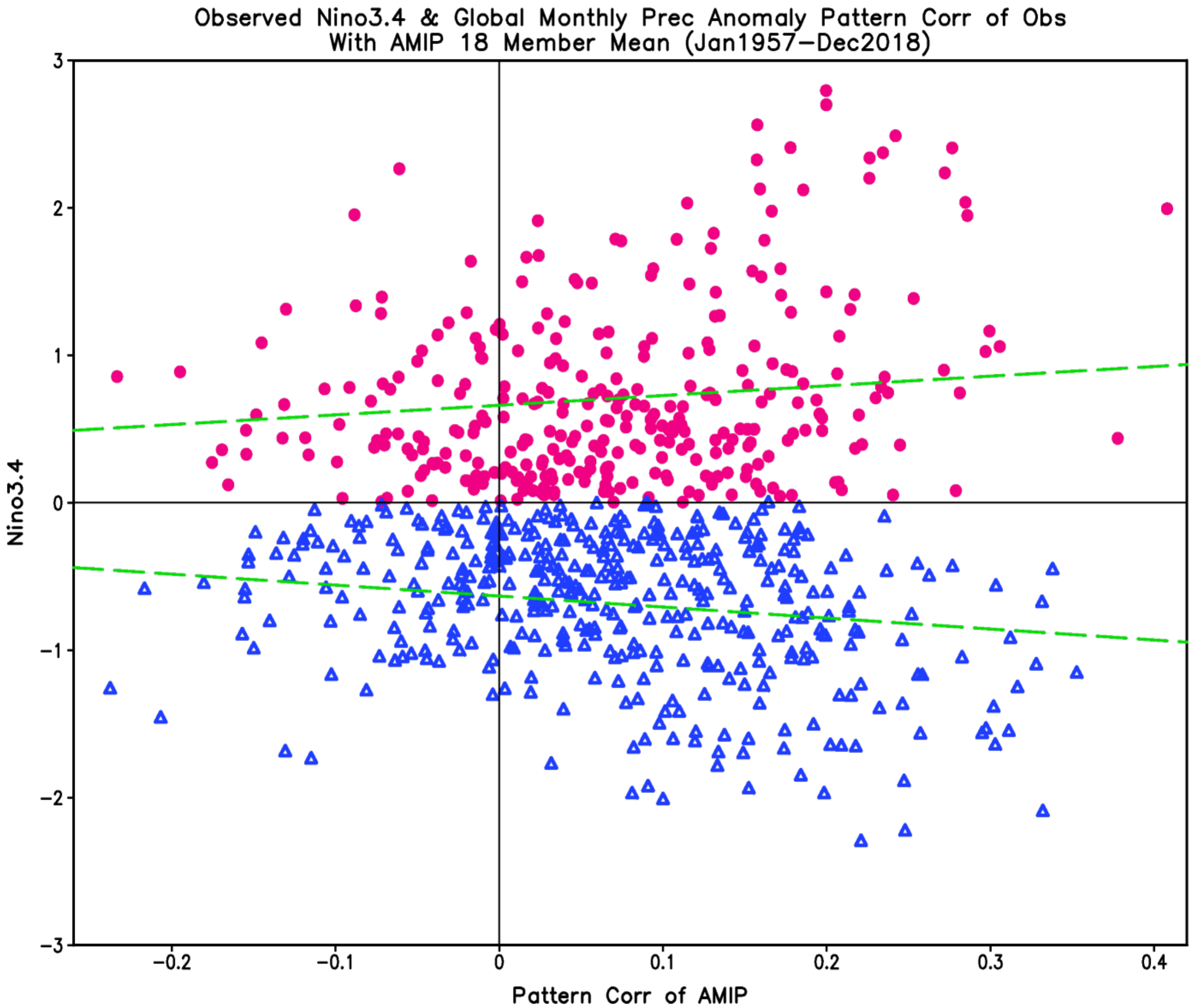

Fig. 9: Scatter plot of pattern correlations of monthly mean precipitation anomalies between observations and ensemble mean of the AMIP simulations in globe land in each month (x-axis) and observed monthly mean Niño3.4 index (y-axis) during January 1957-December 2018. The dished lines represent the linear regression fitting for positive and negative Niño3.4 index, respectively.